



# Unbalance Bearing Fault Identification Using Highly Accurate Hilbert–Huang Transform Approach

**Vishal G. Salunkhe**

Department of Mechanical Engineering,  
Fr. C. Rodrigues Institute of Technology,  
Vashi, Navi Mumbai, Maharashtra 400 703, India  
e-mail: vishal.salunkhe@fcrit.ac.in

**S. M. Khot**

Department of Mechanical Engineering,  
Fr. C. Rodrigues Institute of Technology,  
Vashi, Navi Mumbai, Maharashtra 400 703, India  
e-mail: smkhot@fcrit.ac.in

**R. G. Desavale<sup>1</sup>**

Design Engineering Section,  
Department of Mechanical Engineering,  
Kasegaon Education Society's Rajarambapu  
Institute of Technology,  
Sakhrule, Sangli, Shivaji University,  
Kolhapur, Maharashtra 415414, India  
e-mail: ramchandra.desavale@ritindia.edu

**Nitesh P. Yelve**

Department of Mechanical Engineering,  
Indian Institute of Technology Bombay,  
Powai, Mumbai, Maharashtra 400 076, India  
e-mail: nitesh.yelve@iitb.ac.in

*The dynamic characteristics of rolling element bearings are strongly related to their geometric and operating parameters, most importantly the bearing unbalance. Modern condition monitoring necessitates the use of intrinsic mode functions (IMFs) to diagnose unbalance bearing failure. This paper presents a Hilbert–Huang transform (HHT) method to diagnose the unbalanced rolling bearing faults of rotating machinery. To initially reduce the noise levels with slight signal distortion, the noises of the sample in normal and unbalanced fault states are measured and denoised using the wavelet threshold approach. The complex vibration signatures are decomposed into finite IMFs with ensemble empirical mode decomposition technique. Fast Fourier techniques are employed to extract the vibration responses of bearings that are artificially damaged using electrochemical machining on a newly established test setup for rotor disc bearings. The similarities between the information-contained marginal Hilbert spectra can be used to diagnose rotating machinery bearing faults. The data marginal Hilbert spectra of Mahalanobis and cosine index are compared to determine the fault indicator index's similarity score. The HHT model's simplicity enhanced the precision of diagnosis correlated to the results of the experiments with weak fault characteristic signals. The effectiveness of the proposed approach is evaluated with several theoretical models from the literature. The HHT approach is experimentally proven with unbalance diagnosis and capable of classifying marginal Hilbert spectra distribution. Because of its superior time-frequency characteristics and pattern identification of marginal Hilbert spectra and fault indicator indices, the newly stated HHT can process nonlinear, non-stationary, and even transient signals. The findings demonstrate that the suggested method is superior in terms of unbalance fault identification accuracy for monitoring the dynamic stability of industrial rotating machinery.*

[DOI: 10.1115/1.4062929]

**Keywords:** Hilbert–Huang transform, fast Fourier techniques (FFT), unbalance bearing fault, marginal Hilbert spectra, fault indicator indices

## 1 Introduction

For precise fault identification of rotating machinery, a rolling element bearing's (REB) vibration response is crucial. The vibration response of REB is influenced by several variables, including failure, radial clearance, unbalance, and lubrication. One of the most pressing problems is bearing failure. As a result, it has recently received increased attention from scientists and engineers. The primary rolling element bearing fault is divided into two categories: localized defect and distributed defect. In rotating machinery, the rotor-bearing system is often retained and regulated under challenging situations such as high rotational speed and overload. The impacted contact area can cause high-stress levels of a few gigapascals even with a minimal load between the rolling element and

raceway [1], possibly resulting in local faults [2]. As a result, vibration response of defective parts is transferred through its mated components, and a vibration signal is produced that can be utilized to identify flaws. Fault detection can be viewed as a preceding step of fault diagnosis. Therefore, identifying bearing defects is crucial to adhere to industrial engineering [3].

Initial detection of bearing failure reduces maintenance costs and assures safer and more enduring machinery operation. The vibration signals close relationship to the equipment design makes fault diagnosis technology more widely applicable [4]. In general, rolling bearing failure detection technology is divided into three stages: signal acquisition and processing, feature extraction, and fault diagnosis identification. The foundation for the study is set by signal collection and processing, among others. The final phase in fault diagnosis is extraction, which is essential. The goal of fault feature extraction is to take high-dimensional data and turn it into low-dimensional information about its underlying features. Its core consists of pattern recognition and feature extraction being a

<sup>1</sup>Corresponding author.

Manuscript received March 3, 2023; final manuscript received July 4, 2023; published online July 26, 2023. Assoc. Editor: Weinbin Li.

crucial initial step. Online incipient failure detection has emerged as a significant challenge for prognostics and health management of rotating machinery due to the rapid growth of sensor technology. There are substantial theoretical and clear engineering criteria for online incipient defect detection of bearings. As a result, it creates many problems, including dimension disaster, category unbalances, a lack of labeled sample data, a scarcity of valuable data, and improper industry data samples. In response, the technology for data-driven intelligent defect diagnostics is developed. From a substantial quantity of industrial data, it is possible to extract relevant diagnosis information, ultimately used to improve or aid the diagnosis process. The model-based technique can convert complex engineering problems into simplified mathematical models [5]. The model-based theoretical approach builds the circumstances for the effectiveness of experiments and evaluation of mathematical models with experimental results. Therefore, the model-based vibration conditioning monitoring techniques have been to pick up in-depth study throughout the earlier decades. Using signal processing techniques makes it feasible to attain significant characteristic frequency from the vibration signals. The present work uses the innovative technique of model-based study to determine the effect of speed, load, bearing fault, and other physical parameters on bearing failure [6].

Wu et al. [3] illustrated the looseness of rotating machinery based on the Hilbert–Huang transform (HHT) approach. Complex vibration signatures are decomposed and integrated with intrinsic mode function (IMF) and empirical mode decomposition (EMD). Marginal Hilbert spectra with fault index are used to find the similarity among information for accurate diagnosis of looseness fault in the machinery. Rai and Mohanty [4] investigated the potential for subjectivity error in characteristic defect frequencies of bearings based on Hilbert transform (HT) in the time domain feature. The effectiveness of HT is maximized in the frequency domain by integrating IMF with HHT. Wang et al. [7] developed noise based technique by combining HHT and support vector machine (SVM). The wavelet packet measures and denoises the sampling engine in fault states by lowering the noise level with barely perceptible signal distortion. Huang et al. [8] developed technique for non-stationary nonlinear data analysis based on time scale. Based on a local signal, IMF uses the instantaneous frequency to eliminate artificial harmonics. Wu and Huang [9] illustrated using ensemble empirical mode decomposition (EEMD) to sift through a group of white noise-added signals to find the mean true result. White noise with finite as compared to infinitesimal amplitude scales signals for IMF collection using the dyadic filter provided feasible solutions in the sifting process. Ibn and Sinha [10] presented an influence coefficient balancing technique for two planes with reduced sensor.

Yu et al. [11] investigated Shannon entropy and HHT for gear fault detection based on energy-frequency-time distribution with probability distribution. Song et al. [12] obtained an improved gray wolf optimization with adaptive sparse contractive auto-encoder for unbalanced bearing faults. Optimizing sparse coefficient based on homotopy regularization with sparse graph embedding for extracting fault features. Faulty sample sparse data are compensated with improved tent chaotic mapping for gray wolf optimization. Zhang et al. [13] presented a nonlinear model based on D’Alembert’s principle for turbochargers of floating ring bearings. Poincare mapping, trajectory analysis, bifurcation behavior, and frequency domain responses are investigated for avoiding fluid-induced instabilities with unbalance effects. Liu et al. [14] proposed HHT for bearing fault detection by combining Elman neural network and singular value decomposition for extracting feature vector. Shinde and Desavale [15] illustrated unbalance and misalignment in rotating machinery based on dimension theory and SVM. Numerical results are effectively in line with experimental findings for classifying the accuracy of faults with minimum error for high-speed machines.

Li and Zhang [16] investigated a supervised locally linear embedding projection (SLLE) technique for fault identification in machinery. Fault classification performance significantly improved using the SLLE approach. McFadden and Smith [17,18] developed a

numerical model for rolling element bearing operating in radially loading conditions for predicting the inner defect. Defects are modeled as spectrum caused by roller passage frequency for the inner race. Patil et al. [19] formulated analytical model for bearing rollers and races as nonlinear spring. Numerical algorithm simulates the defect of races and rollers in the frequency domain. Dick et al. [5] illustrated a quasi-static load distribution and stiffness of roller bearing with outer and inner race defects with variation in length and surface roughness. Igarashi and Kato [20] investigated vibration characteristics of bearings with numerous dents on races. Radial velocity of outer race is evaluated by means of moving coil converter. Sopanen and Mikola [21,22] formulated a model of 6DOF for spherical roller bearing by considering diametral clearance effects. Low-ordered waviness and roundness are significant factors for the influence of vibration characteristics. Tandon and Choudhary [23] developed an empirical model for the analysis of discrete spectrums for defect identification. The gradual increment in vibration amplitudes leads to increased machine vibrations with higher frequency. Tandon and Choudhary [6] illustrated a numerical model to predict the bearing signature under radially loading conditions due to unevenly distributed defects. The model foretells discrete spectrum responses at both inner and outer ring defect frequencies. Choudhury and Tandon [24] considered vibrations of bearing with different defect sizes. The 3DOF system is modeled for the rotor-bearing system. The sideband peaks at defect frequencies, cage frequencies, and shaft frequencies, are predicted using their model.

Tomovic et al. [25] illustrated a realistic novel vibrating model for a sturdy rotor-bearing structure with bearing clearances. Desavale et al. [26,27] applied dimensional analysis to model vibrational problems due to local flaws in the forced draft fans bearings. Taguchi technique is used to carry out a multivariable regression analysis. Experimental results with numerical models using dimensional analysis compared and found close agreement. Desavale et al. [28,29] investigated the consequences of rotating speed, radial load, with various other factors on vibration responses by building a model for the rotor-bearing structure. Mathematical models using non-dimensional parameters are developed to analyze the rotor-bearing structure. Mufazzal et al. [30] developed lumped system with 2DOF with multi-impact theories for simulating healthy and defective bearings. Patil et al. [31] illustrated a dynamic model for a circular and square defect on bearing raceways for high-speed application in a sugar mill. Kanai et al. [32] developed a novel and condensed method for spherical roller-bearing failure diagnosis by an artificial neural network. Patel et al. [33] presented a dynamic model for the investigation of the vibrations of deep groove ball bearings (DGBB) with single and multiple surface flaws on both raceways.

Jing [34] obtained an analytical model for contact zone excitation for raceway faults in roller bearings. The slicing technique is integrated with an analytical method for stiffness analysis of outer race profiles. Linkai et al. [35] illustrated an empirical model based on multiple impulses generated around the races due to contact forces and slippage action. Rafsanjani et al. [36] examined a statistical model to predict bearing vibration characteristics due to surface fault. Diverse nonlinear dynamic conditions forecast the presence of surface pitting at corresponding characteristic frequencies in bearing. Rui et al. [37] investigated an analytical model with varying compliance vibration responses in the different speed ranges, number of balls, and rotor eccentricities. Jadhav et al. [38] demonstrated the power of dimension theory to detect distributed defects in bearing. Kumbhar et al. [39,40] presented a dimension theory with thermal parameters for fault identification in high-speed roller bearings for industrial machinery. Classification accuracy with different fault indexes with the speed of the rotor analyzed for avoiding catastrophic failure. Multivariable regression analysis is evaluated to identify exact bearing failure and the efficacy of the theoretical model. Salunkhe et al. [41] formulated a model based on dimensional analysis using a matrix technique to forecast the vibrations associated with dependent parameters. Shinde et al. [42] studied the extracted features of vibration response from rotor-

bearing structure by using the K-nearest neighbor network algorithm for multiple fault classification. Patil et al. [31] investigated square and circular defect vibration characteristics by empirical mathematical model under different conditions. Vishwendra et al. [43] illustrated K-nearest neighbor for rolling bearing fault detection by considering varying speed and radial loading conditions.

In all the above studies, HHT is utilized as an effective preceding step of fault diagnosis. The commonly used technique in the existing process monitoring methods, such as vibration analysis, envelope analysis, machine learning and artificial intelligence, and acoustic emission. The identification of unbalanced bearing faults in industries can still pose several challenges. Some of the existing problems like signal interference, sensitivity to operating conditions, integration with maintenance strategies, limited accessibility, and complex machinery. However, motivated by the above analysis no research published to date that presents an effective HHT method for unbalance fault identification. To diagnose the unbalanced rolling bearing faults of rotating machinery, this is the advanced state-of-the-art of the present work. This research contributes to the use of HHT modeling for the detection and classification of incipient bearing failures. This is the first study in the realm of roller-bearing diagnosis that synchronizes the robustness and accuracy of HHT.

A literature review indicates that HHT distinct mathematical models have been used extensively for vibration analysis of industrial machines. Simple mathematical models cannot represent a complex industrial system. Hence, many studies reported the potential of HHT due to its simple and unique combination of analytical with the experimental approach for predicting the vibration characteristics. Even mathematically modeled well, they cannot expose the critical nonlinear or anisotropic material characteristics encountered generally in practice. Hence, HHT is used to investigate the effect of the unbalance bearing fault in a DGBB. First, HHT model formulation is presented, subsequently stimulating the vibrational characteristics. The information-containing IMFs are then combined to generate the marginal Hilbert spectra, which are obtained using the Hilbert transform. Fault indicator index measures similarities between information-contained marginal Hilbert spectra of vibration signals. The estimated routine performance of the developed HHT model is compared with the experiments. Experimental investigations verify the prediction of vibration characteristics using HHT for incipient fault classification. The proposed method takes into account the influence of noise on detection and fully excavates incipient fault information. The results demonstrated that the suggested approach is capable of identifying the unbalanced bearing faults at rotating equipment by comparing the similarity in marginal Hilbert spectrum distributions. Finally, the conclusion and scope for future work are revealed.

## 2 Hilbert–Huang Transform for Unbalance Bearing Fault

**2.1 Empirical Mode Decomposition.** Huang 1998 created the innovative tool HHT for data analysis for various applications. The complex nonlinear and non-stationary signals are divided into a limited number of IMFs using the HHT algorithms EMD approach. The function that fulfills both requirements is known as IMF. Across the entire set of data, the frequency of extrema and zero must be identical or a maximum of one difference. The mean value of the envelopes formed by the local maxima and minima is always zero. The technique is to break down a complex signal into wavering parts and a monotonous pattern. In each IMF, only one frequency exists at any given time. Consequently, any complex signal  $x(t)$  is given as [3]

$$y(t) = \sum_{k=1}^m d_k(t) + s_m(t) \quad (1)$$

where  $d_k(t)$  is the  $k$ th IMF of the signal  $y(t)$  and  $s_m(t)$  is the residue, which can be signal mean trend. The IMF can be a solitary

amplitude component and frequency modulation signal due to the two parameters of each IMF. The EMD process can break down complex nonlinear non-stationary signs, but it still leaves several problems unresolved. One of them is the occurrence of different frequencies being in a single IMF. Signal intermittency is the major cause of mode mixing and may be misinterpreted as having different physical meanings [3]. Each IMF is mathematically orthogonal to the others. No leakage of energy from one IMF to neighboring ones because all the IMFs are autonomous. Due to the mode mixing concern, the fundamental principle may be violated. The end effect, which results in a drift at end of the signals with limited lengths, is the other challenge. Wu and Huang introduced a novel noise analysis approach ensemble EMD to address the shortcomings of the original EMD [9]. The original measured signal and the random white noise created in this new method make up the  $j$ th artificial measurement  $y_j(t)$  can be written as [9]

$$y_j(t) = y(t) + w_j(t) \quad (2)$$

The  $j$ th simulated measurement is then decomposed into IMFs using the original EMD approach

$$y_j(t) = \sum_{k=1}^m d_{kj}(t) + s_{mj}(t) \quad (3)$$

With numerous repetitions of these steps, the corresponding IMF is

$$d_k(t) = \sum_{j=1}^{N_c} \frac{d_{kj}(t)}{N_c}, \quad k = 1, 2, \dots, m \quad (4)$$

$$s_m(t) = \sum_{j=1}^{N_c} \frac{s_{mj}(t)}{N_c}$$

where the EEMD process is  $N_c$  and the number of IMFs is  $m$ . To create a space, the additional EEMD white noise offers an even distribution reference scale. In contrast to the original EMD approach, the EEMD technique used to address the aforesaid limitations [9]. Even though the EEMD method only requires two parameter noise amplitude and ensemble number to separate the important components from the signals [9]. A low signal-to-noise ratio has no impact on decomposition. As higher the ensemble number in the EEMD, white noise cancels in the IMFs means. Based on statistical criterion minimal ensemble number  $N_c$  is calculated as follows [1]:

$$N_c = \frac{\varepsilon^2}{\varepsilon_n^2} \quad (5)$$

where  $\varepsilon$  is the added noise amplitude and  $n$  is the standard deviation. The EEMD process ensemble mean values are not always the IMFs. The associated Hilbert spectra for certain components might have an alias, thereby making it difficult to analyze these components using the Hilbert spectrum. A comprehensive approach by post-processing the EEMD component with the EMD methodology is used to overcome drawbacks. The integrated technique begins by decomposing the new measurement using the EEMD method can be defined as follows [9]:

$$y(t) = \sum_{k=1}^m [i_k(t)] + p_{m+1}(t) \quad (6)$$

where  $i_k(t)$  and  $p_{m+1}$  are the  $k$ th component respectively. The  $k$ th component is known as the  $k$ th pseudo-IMF since it might not be the IMF. Second, the first pseudo-IMF  $i_1(t)$ , is split into two parts using the original EMD with frequency scales and residue. The first component controls the first pseudo-IMF  $i_1(t)$ , and fits IMF, thus first IMF  $d_1(t)$  is given as

$$i_1(t) \rightarrow d_1(t) + p_1(t) \quad (7)$$



where  $p_1(t)$  is the  $i_k(t)$  remainder after extracted IMF  $d_1(t)$ . To create the consecutive new signal  $E_k(t)$ , the residues from every pseudo-IMF  $p_{k-1}(t)$ , are added to the subsequent pseudo-IMF  $i_k(t)$ . The consecutive new signal  $E_k(t)$ , based on EMD is classified into the  $k$ th IMF,  $d_k(t)$  and the residue

$$E_k(t) = i_k(t) + p_{k-1}(t) \rightarrow d_k(t) + p_k(t), \quad k = 2, 3, \dots, m \quad (8)$$

The IMF  $d_1(t)$  to  $d_m(t)$  can be retrieved by repeating the steps and the final residue is

$$s_m(t) = p_m(t) + p_{m+1}(t) \quad (9)$$

The mode mixing and end effects are all retained by the integrated method. The energy leakage from one mode to another is due to a mode mixing problem. An orthogonality criterion can be utilized to measure the leakage in energy of two IMFs. The leakage of IMFs energy is measured by using the index of orthogonality [8]. The values of the orthogonality measurement indices can be positive or negative. As a result, these values may cancel each other out, yielding small indices. To evaluate the independence of all IMFs the orthogonality index,  $i$ th and  $k$ th IMFs is given as [9]

$$\beta = \frac{\left( \sum_{j=1}^N d_i(j) d_k(j) \right)^2}{\left( \sum_{j=1}^N d_i(j)^2 \right) \left( \sum_{j=1}^N d_k(j)^2 \right)} \quad (10)$$

where  $N$  is the IMF length.

**2.2 Signal Denoising and Marginal Hilbert Spectrum.** Inevitably, throughout the measurement process, certain additive noises, background interferences, and the hardware of the measurement system distorted the recorded signals. For model accuracy, signals must be denoised. Least squares, matching pursuit, spectral subtraction, and wavelet threshold approaches are utilized successfully in applications to reduce noise [10]. The denoising technique is divided into three steps: signal decomposition, threshold determinations, and signal reconstruction. The enumerated and chosen parameters are: three level Daubechies wavelet “db4,” the threshold signal  $sig(x)(x) - t$  if  $x > t$ , where  $t$  is a threshold  $t = \{2 \log(len f)\}^2 f$  is frequency. As an illustration, Fig. 1 displays the denoised signal of  $-1$  to  $1$ . Since the white noise components are controlled, the original signal is retained in the denoised signal.

A steady reference frame for the decomposition is established by the white-noise series in the EEMD. In order to separate the

information-containing IMFs from the non-information-containing noise, the energy density is utilized. The  $k$ th IMF is defined as

$$F_k = \sum_{j=1}^n \left\{ \frac{(d_k(j))^2}{N} \right\} \quad (11)$$

The normalized white-noise series’ Monte Carlo verification reveals the statistical correlation.

$$\ln \bar{F}_k + \ln \bar{U}_k = 0 \quad (12)$$

For  $k$ th IMF,  $\bar{F}_k$  and  $\bar{U}_k$  are the energy density and period function. It demonstrates that the white-noise series for energy density will resemble a straight line. To allow for the distribution deviation, two lines of spread with varying confidence levels are developed [3]

$$\ln \bar{F}_k = -\ln \bar{U}_k \pm \alpha \sqrt{\frac{2}{N}} e^{\ln \frac{\bar{U}_k}{2}} \quad (13)$$

where  $\alpha$  is the normal distribution. If the energy density-period relationship of the IMFs is similar to that of white noise, then these IMFs represent the least information-contained signal. The significance test used to extract the information-containing IMF  $d_k(t)$ . Applying the Hilbert transform to the IMF component yields the complex-valued analytical signal  $z_k(t)$  [8]

$$z_k(t) = d_k(t) + ih\{d_k(t)\} = B_k(t)e^{i\beta(t)} \quad (14)$$

The Hilbert transform of  $d_k(t)$  represented by  $h\{d_k(t)\}$ , defined by  $p.v.$  as the Cauchy principal value [3]

$$\widehat{d_k}(t) = h\{d_k(t)\} = p.v. \int_{-\infty}^{\infty} \frac{d_k(\tau)}{\pi(t - \tau)} d\tau \quad (15)$$

For functions that are defined in  $L^P$ -space are present in the transform [3]. The frequency  $f_k(t)$  which is time-dependent can be calculated using the  $a_k(t)$ , and  $d_k(t)$  respectively.

$$f_k(t) = \frac{d}{dt} \left\{ \tan^{-1} \frac{\widehat{d_k}(t)}{d_k(t)} \right\} \quad (16)$$

The Hilbert spectrum is the information-contained IMFs time-frequency-energy or amplitude distribution, derived in terms of  $f_k(t)$  and  $a_k(t)$  is given as [9]

$$H[f, t] = \sum_{\varphi}^n a_k(t) \exp \left( i \int f_k(t) dt \right) \quad (17)$$

The information-contained IMFs index set is represented by  $\varphi$ . The time integration of  $H[f, t]$  yields the information-contained marginal Hilbert spectrum.

$$S(f) = \int_0^T H[f, t] dt \quad (18)$$

Therefore, the characteristics of the unbalance bearing fault that are hidden in the complex vibration signals can be seen using marginal Hilbert spectra [44].

### 3 Distribution Measurement for Unbalance Classification

Based on similarity measurements between marginal Hilbert spectrum distributions, a method for identifying unbalanced faults in rotating machinery has proposed. In the proposed technique, the similarity between two data sets is first assessed using the statistical notion of Mahalanobis distance [3]. The distribution vectors  $S_i$  and  $S_j$  of the marginal Hilbert spectra are separated by an

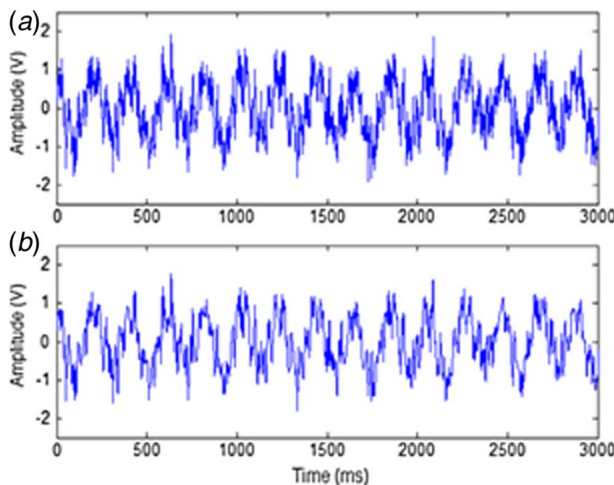


**Fig. 1 Denoising of bearing noise signal: (a) original signal and (b) denoised signal**

M-distance index, defined as follows [9]:

$$V_{ij} = \left\{ (S_i - S_j)^T \sum_{ij}^{-1} (S_i - S_j) \right\}^2 \quad (19)$$

The covariance matrix of  $S_i$  and  $S_j$  is represented by  $\sum_{ij}^{-1}$ . The statistical interpretation makes it evident that if the M-distance index is minor, the two distribution vectors will be closer in similarity. The cosine index to measure two vectors' similarity marginal Hilbert spectra is given as

$$\delta_{ij} = \frac{\sqrt{S_i^T S_j}}{S_{i2}^2 S_{j2}^2} \quad (20)$$

If the cosine index is higher, the two marginal Hilbert distribution vectors are more parallel and comparable. The M-distance index trend runs counter to the cosine index trend. In other words, if the M-distance index is lower but the cosine index is higher, the two vectors are more similar. The M-distance and cosine index combined with this observation to create the fault indicator index, improving the similarity measurements.

$$\sigma_{ij} = \frac{V_{ij}}{\delta_{ij}} \quad (21)$$

The lesser the fault indicator index, the more identical the distribution vectors are. The flowchart of Hilbert–Huang transform with integrated EEMD is shown in Fig. 2. The objective function specified in Eq. (19) is denoted by  $S(f)$ , and  $d_k(t)$  is the signal after  $k$  sifting iterations.  $s_m(t)$  stands for the envelope mean signal of  $d_k(t)$  and  $\varepsilon_n$  at the start of EEMD initializes the residual signal  $\varepsilon$  by subtracting the preceding IMF. In the EEMD, an inner loop is contained within an outer loop, forming a nested loop structure.

#### 4 Experimental Platform

As shown in Fig. 3, an experimental test rig was employed to produce the vibration signals used in this work. This test rig includes a variety of attachments for introducing faults. The significant parts of the test rig are a three-phase induction motor of 2HP, a modular coupler, a flexible coupling, two pedestal blocks, two deep groove ball bearings, a motor controller variable frequency drive (VFD), and a radial load. A vibration isolation mounting is provided for supports the system. The base support of the induction motor is the closest, and the second support is another end at a distance of

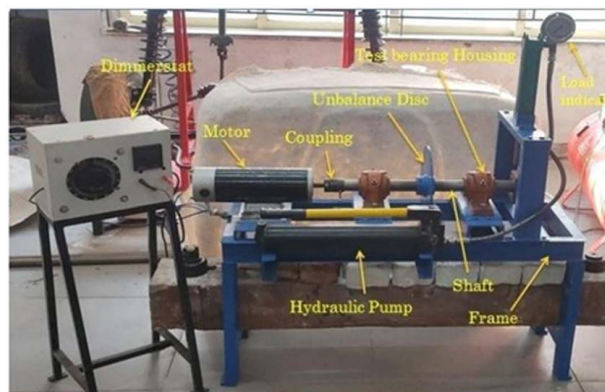


Fig. 3 Experimental test rig

1.5 m. The flexible foundation is supported by two DGBB bearings mounted on the shaft, with one disc located 745 mm away from the flexible coupling. The discs are 20 mm thick and have an outside diameter of 130 mm. They have staggered threaded holes (M5) with two distinct pitch diameters of 70 mm and 120 mm. Each pitch diameter has an angle of 30 deg between the two adjoining holes. Table 1, ten cases of unbalance bearing fault are demonstrated for experiment. A circumferential loader is placed in the center of two bearing blocks to impose radial load on the testing bearings. A VFD is employed to control the rotor shaft speed from 750 rpm to 3000 rpm. To measure vertical and horizontal vibrations, an accelerometer with a sensitivity of 110 mV/g is attached to the far bearing housing. The Adash 1000 (FFT) analyzer collects and processes vibration signatures. Ten machine run-ups are performed with nine unbalance cases. The machine speed was increased linearly for each of the ten run-ups, from 750 rpm (5 Hz) to 3000 rpm (50 Hz) over 135 s. Table 1 lists the various masses added to both balance planes at a constant radius of 5 cm for the various runs.

When the rotor system is operational, the time-frequency spectrum can indicate the regularity of frequency change [45]. Figure 4 depicts the time-frequency spectrum of several running stages acquired by the original HHT. Figures 4(a)–4(c) depict the time-frequency spectrum of the normal, bearing fault, and unbalanced operating states. The unbalance running state instantaneous frequency oscillates between 15 Hz and 38 Hz, as shown in Fig. 4(c).

#### 5 Experimental Results and Discussions

**5.1 Decomposition Into Intrinsic Mode Functions.** To evaluate the proposed approach for diagnosing unbalanced bearing faults in rotating machines, the various experimental scenarios of unbalance are demonstrated using a simple rotor-bearing test bed arrangement. Ten cases of unbalanced bearing failure are illustrated for experimentation, as shown in Table 1. Case 0 depicts the test bed in a balanced, healthy working condition, while cases 1–10 show an unbalance bearing fault. Similar operating conditions were applied in each of the ten cases as the motor drives the rotor-bearing system at a constant speed between 750 rpm and 3000 rpm. A total of 600 time series data sets are collected by ten times. The decomposition of the 600 data sets is carried out using the integrated EEMD approach. The ensemble number in this process is 150, and the amplitude of white noise EEMD method is 0.12 times the original signal. To fix the mode mixing issue and end effect, the EEMD approach includes additional white noise. However, as indicated in Eq. (5), a significant white noise necessitates ensembles, which increases the computational effort. As a result, the criteria for choosing the white noise level are to establish the minimum white noise amplitude to enhance the mode mixing criteria. Ten IMFs and a trend of different frequency bands are created from the complex vibration signal. A similar data set as in Fig. 5 is used to illustrate the superiority of the combined

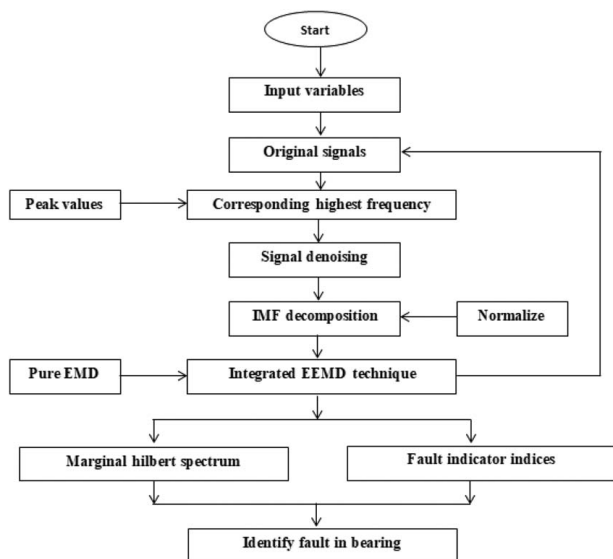
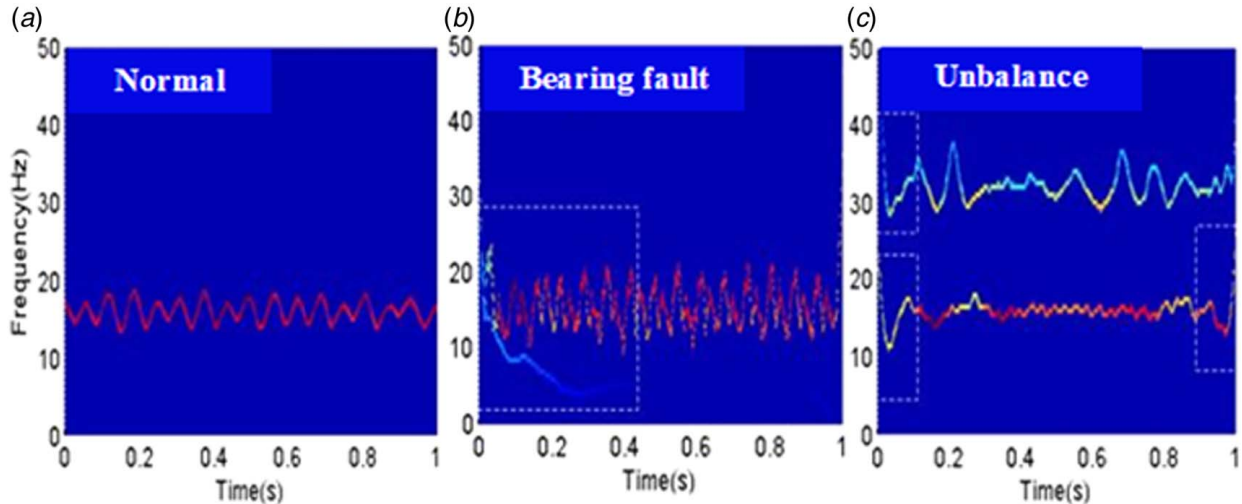


Fig. 2 Flowchart of Hilbert–Huang transform

**Table 1 Cases of unbalance**

Condition	Total run	Unbalance tolerances	
Case 1	0-run	2 g × 5 cm @ 30 deg = 20 gcm @ 30 deg	$\epsilon_{1,0}$
Case 2	1-run	6 g × 5 cm @ 60 deg = 44 gcm @ 60 deg	$\epsilon_{1,0} + \epsilon_{1,1}$
Case 3	2-run	4 g × 5 cm @ 60 deg = 32 gcm @ 60 deg	$\epsilon_{1,0} + \epsilon_{1,2}$
Case 4	3-run	6 g × 5 cm @ 30 deg = 44 gcm @ 30 deg	$\epsilon_{1,0} + \epsilon_{1,3}$
Case 5	4-run	4 g × 5 cm @ 180 deg = 20 gcm @ 180 deg	$\epsilon_{1,0} + \epsilon_{1,4}$
Case 6	5-run	4 g × 5 cm @ 330 deg = 20 gcm @ 330 deg	$\epsilon_{1,0} + \epsilon_{1,5}$
Case 7	6-run	2 g × 5 cm @ 90 deg = 20 gcm @ 90 deg	$\epsilon_{1,0} + \epsilon_{1,6}$
Case 8	7-run	2 g × 5 cm @ 30 deg = 20 gcm @ 30 deg	$\epsilon_{1,0} + \epsilon_{1,7}$
Case 9	8-run	4 g × 5 cm @ 120 deg = 20 gcm @ 120 deg	$\epsilon_{1,0} + \epsilon_{1,8}$
Case 10	9-run	2 g × 5 cm @ 90 deg = 32 gcm @ 90 deg	$\epsilon_{1,0} + \epsilon_{1,9}$



**Fig. 4 Actual time-frequency spectrum for (a) normal, (b) bearing fault, and (c) unbalance**

EEMD over the pure EMD technique. Table 2 lists the orthogonality indices  $\beta_{ik}$  analogous to various IMFs from the identical data set in Fig. 5. The mean value of all 600 sets of orthogonality indices is 0.00213, ensuring IMF independence.

The sixth IMF4 is to have different frequencies in pure EMD. The IMF5 and IMF7 frequency scales are included in this IMF component. Consequently, as illustrated in Fig. 5 IMF4, the usage of the integrated EEMD approach is primarily to overcome this mode

mixing problem. The integrated EEMD approach, on the other hand, causes the instantaneous frequency of IMF4 to modulate with the 25 Hz mean frequency and has less variance. Figure 6 displays all 600 data sets IMFs energy density-period distributions. The confidence level spread lines are to be the first lower and 99th upper confidence limits, with the value of Eq. (13) being 2.326. For all data sets in Fig. 5, the same markers denote the same IMF number. The information-contained IMFs are chosen based on marker distribution. In Monte Carlo of the white-noise series verification, all IMFs energy density-period distributions fall between the upper and lower confidence levels. As a result, in Eq. (18), the marginal Hilbert spectra  $S(f)$  is derived by assembling the IMF  $C_1$  to  $C_{15}$ . The ten data sets marginal Hilbert spectra from Eq. (4) provide the reference vector.

Figures 7(a) and 7(b) show the average marginal Hilbert spectra respectively. After establishing the averaged marginal Hilbert spectra for all cases, they are used as the reference vectors for cases 1–7. The tested data in this experiment include two posterior data sets from every case, for a total of 12 data sets. The combined EEMD approach and the significance test are used to compute the 12 tested vectors.

**5.2 Fault Indicator Indices.** The fault indicator indices quantify the similarities between the tested and reference vectors. Equations (19) and (20) determine the fault indicator index  $\sigma_{ij}$  amongst the reference vector  $\bar{S}_i$  and the tested vector  $S_{ij}$  in terms of  $V_{ij}$  and  $\delta_{ij}$ .

Figure 8 presents the estimated fault indicator indices between each reference case and the tested cases. According to the minimal line, each tested case is assigned to the healthy or specific unbalance bearing fault categories corresponding to the reference

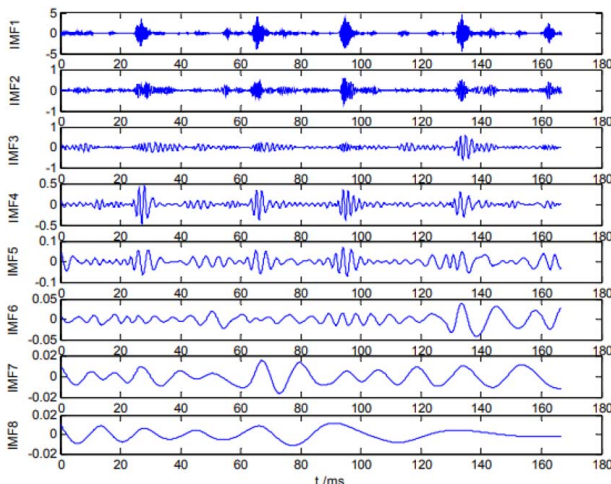


**Fig. 5 IMF plot of vibration signal with integrated EEMD**



**Table 2 IMF orthogonal indices**

$\beta_{ik}$	C1	HC2	VC3	AC4	HC5	VC6	AC7	HC8	VC9
C1	0.0069								
HC2	0.0056								
VC3	0.000186	$5.17 \times 10^{-3}$							
AC4	0.000671	$1.37 \times 10^{-3}$	$1.52 \times 10^{-3}$						
HC5	$4 \times 10^{-6}$	$1.52 \times 10^{-3}$	$3.74 \times 10^{-3}$	$5.64 \times 10^{-3}$					
VC6	$2.12 \times 10^{-4}$	$7.83 \times 10^{-6}$	$5.83 \times 10^{-4}$	$4.94 \times 10^{-4}$	$7.48 \times 10^{-4}$				
AC7	$2.12 \times 10^{-4}$	$2.41 \times 10^{-6}$	$3.41 \times 10^{-5}$	$1.32 \times 10^{-4}$	$5.23 \times 10^{-4}$	$1.26 \times 10^{-3}$			
HC8	$3.47 \times 10^{-4}$	$1.09 \times 10^{-5}$	$1.21 \times 10^{-4}$	$1.27 \times 10^{-5}$	$5.52 \times 10^{-7}$	$1.16 \times 10^{-3}$	$8.45 \times 10^{-2}$		
VC9	$2.29 \times 10^{-7}$	$1.83 \times 10^{-5}$	$2.85 \times 10^{-4}$	$3.50 \times 10^{-4}$	$3.93 \times 10^{-6}$	$1.27 \times 10^{-4}$	$6.51 \times 10^{-2}$	$1.09 \times 10^{-2}$	
AC10	$1.12 \times 10^{-5}$	$6.52 \times 10^{-6}$	$2.58 \times 10^{-6}$	$4.42 \times 10^{-7}$	$1.42 \times 10^{-4}$	$1.34 \times 10^{-3}$	$8.40 \times 10^{-4}$	$1.71 \times 10^{-4}$	$5.54 \times 10^{-3}$

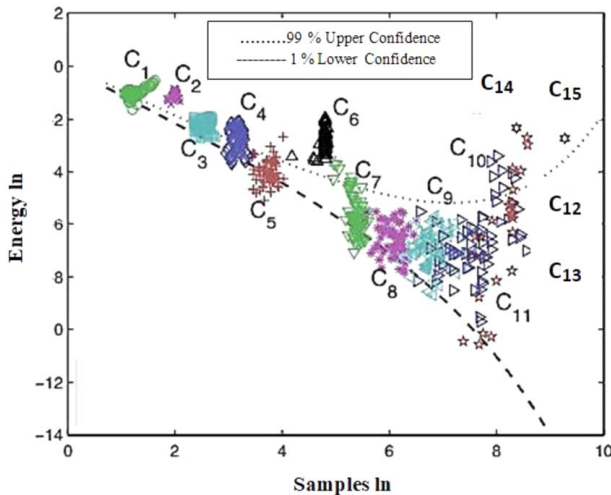


**Fig. 6 Confidence limit test for data sets**

cases on the horizontal axis. The tested case  $S_{32}$  is recognized as case 3 of C3 since the minimum point of line  $S_{32}$  is situated at “3” on the horizontal axis. Table 3 shows the numerical results of the fault indicator indices for the reference and tested vectors. Table 8 shows the reference vectors for cases 1–7 in the top row, the tested vectors in the left column, and the related fault indication indices in the middle array. As shown in Eq. (20), the smaller the fault indicator index, the more likely the tested instance is categorized as the appropriate reference case. The dark blocks in

Table 3 reflect the minimal values among the same rows. It signifies that the tested cases correspond to the reference cases in the top row. Table 3 double-line frames indicate the proper relevant reference cases that are tested. Table 3 results demonstrate that diagnosing faults with greater than 92% accuracy can be accomplished by measuring fault indicator indices among marginal Hilbert spectra. Additionally, with the significance test, the marginal Hilbert spectrum composed of the IMF C1–C8 is generated for diagnosis and comparison, as shown in Table 3. Out of the total 12 tested cases, 11 cases are identified correctly. In other words, the significance test and the selection of information-contained IMFs can improve the accuracy of diagnosis. Finally, the proposed approach is feasible for detecting unbalance in rotational machines.

**5.3 Unbalance Bearing Vibration Response of Intrinsic Mode Functions.** The vibration spectrum is gathered in three different experiments using a piezoelectric accelerometer mounted on a bearing pedestal. 24,500 Hz and 1 s are the sample frequency and time, respectively. An initial test is performed on the healthy bearing. Table 4 lists relevant data on the bearing parameters. For each type of experiment, the shaft is rotated at varied speeds of 750, 1500, 2000, and 3000 rpm. The vibration fault characteristics frequencies for 750, 1150, and 1500 rpm shaft speeds are shown in Table 5. The IMFs of bearing with no fault with FFT are shown in Figs. 9(a) and 9(b).

Figures 9(a) and 9(b) show that a period of 0.02 s is equivalent to a frequency of 5 Hz, close to the fundamental train frequency of 11.5 Hz with healthy bearing. For each case, the findings are explained below. The IMFs of vibration signals from four conditions, each exhibiting an unbalance effect, are shown in Figs.

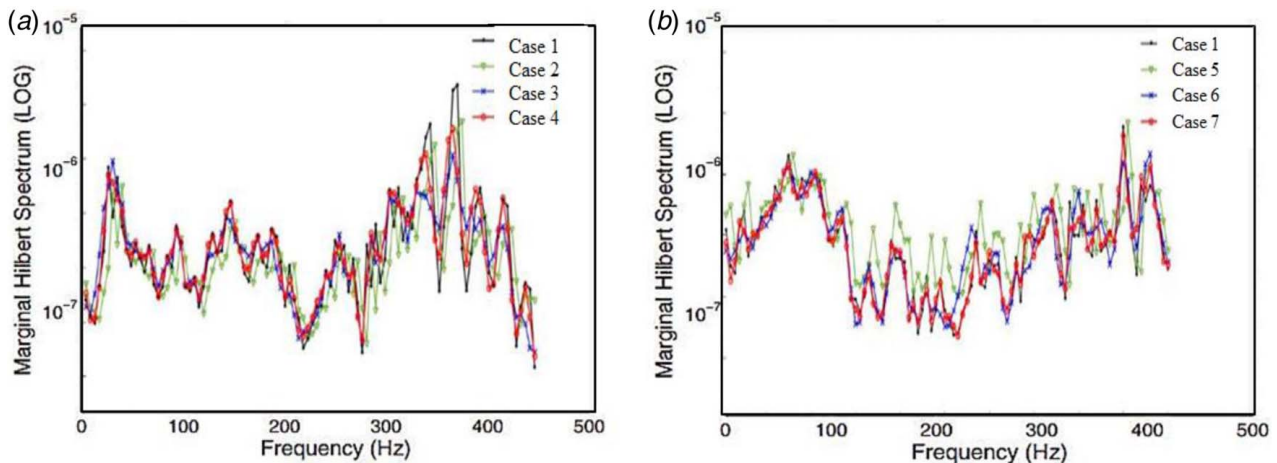


**Fig. 7 Marginal Hilbert spectra (a) cases 1–4 and (b) cases 1, 5–7**

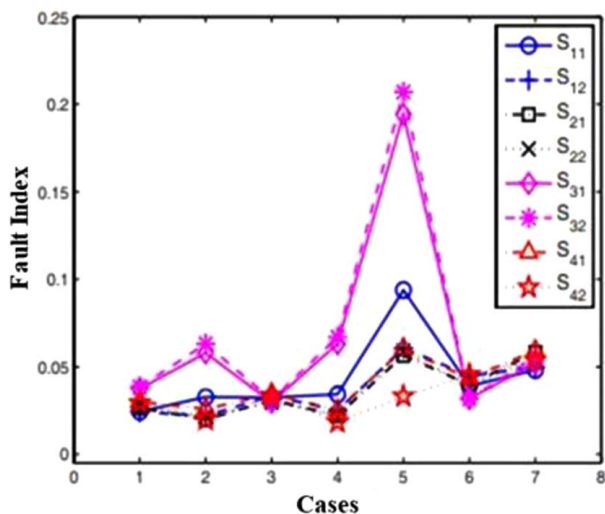


Fig. 8 Fault indicator indices

Table 3 Fault indicator indices C1 to C10

$\sigma_{ij}$	$S_1$	$S_2$	$S_3$	$S_4$	$S_5$	$S_6$	$S_7$
$S_{11}$	0.0154	0.0238	0.0214	0.0246	0.0831	0.0219	0.0325
$S_{12}$	0.0153	0.0128	0.0245	0.0140	0.0542	0.0371	0.0312
$S_{21}$	0.0166	0.0152	0.0278	0.0121	0.0461	0.0278	0.0496
$S_{22}$	0.0179	0.0124	0.0169	0.0119	0.0245	0.0231	0.0478
$S_{31}$	0.0285	0.0481	0.0198	0.0194	0.0142	0.0217	0.0471
$S_{32}$	0.0275	0.0512	0.0245	0.0567	0.0127	0.0152	0.0554
$S_{41}$	0.0131	0.0156	0.0235	0.0524	0.0329	0.0112	0.0512
$S_{42}$	0.0184	0.0132	0.0389	0.0161	0.0261	0.0865	0.0451
$S_{51}$	0.0252	0.0187	0.0311	0.0641	0.0421	0.0874	0.0413

Table 4 Configured bearing parameters

Parameters	Value
Sleeved self-aligning ball bearing	1203 ETN9
Inner side diameter, mm	17
Outer side diameter, mm	40
Width, mm	12
Ball diameter, mm	8
Pitch diameter, mm	48
Number of ball	28
Dynamic load rating (N)	8.84 kN
Max. allowable rotational speed, rpm	24,000

10(a)–10(d). In each case, the IMFs are presented in a time domain and show amplitude variation in each frequency range, with a time and frequency spectrum relating to each IMF. The frequencies in the IMFs are in decreasing order, with IMF1 having the highest frequency content and the highest maximum

rate of amplitude change. The final IMF4 indicates fluctuations at the slowest rate, reflecting the vibration signal lowest frequency. IMF1 seems almost identical to the original signal in Figs. 10(a)–10(d) because it displays the highest frequencies of the signal. As a result, the FFT of IMFs has been added to the existing HHT approach to precisely detect the defect frequency present in vibration signals from faulty bearings, as illustrated in Figs. 11(a)–11(d). The IMF in the case of an outer race defect with FFT is shown in Figs. 12(a) and 12(b). Correspondingly IMF in case bearing of inner race defect with FFT is shown in Figs. 13(a) and 13(b). Another crucial finding is that the self-adaptive EEMD process only produced four IMFs for a precise diagnosis of bearing defects. Due to the frequency content in vibration signals from defective bearings when impulses are present, the frequency range and energy level are raised. The rotor of the bearing is loaded with 200 N radial load and bearing rotated at 750, 1500, 2000, and 3000 rpm. Vibration velocity of 18 mm/s, acceleration  $g = 0.577 \text{ m/s}^2$  at frequency of 12 Hz, and velocity of 12.2 mm/s,  $g = 15.8 \text{ m/s}^2$  at frequency of 24 Hz. Similarly, velocity of 4.02 mm/s,  $g = 5.39 \text{ m/s}^2$  at frequency of 39 Hz, and velocity of 8.55 mm/s,  $g = 7.31 \text{ m/s}^2$  at 57 Hz with IMFs are shown in Figs. 10 and 11. Further which are close to the unbalance defect frequency  $1 \times \text{RPM}$ , respectively. Similarly for outer race frequency increase to 65 Hz with vibration amplitude of 9.98 mm/s,  $g = 11.1 \text{ m/s}^2$  at 3000 rpm as in Fig. 12. Inner race frequency increases up to 130 Hz with vibration amplitude of 9.07 mm/s,  $g = 17.1 \text{ m/s}^2$  at 3000 rpm which clearly indicates bearing fault frequency exists at  $3 \times \text{RPM}$  and more as shown in Fig. 13. Figure 14 illustrates axis orbits of the unbalance are different from normal operating status and bearing fault status. Therefore, the FFT of IMFs from the HHT process utilizes the efficiency of the Hilbert transform to determine accurate frequencies of the rolling element bearing.

**5.4 Comparison of Experimental Results.** The fault diagnosis method realizes the accurate diagnosis and location of the unbalance in the rotor-bearing system. It can be seen that when speed rises, the vibration amplitude for the outer race increases. For the several loads, a distributed outer race fault results in a lower vibration amplitude at all RPMs than a local outer race fault. The vibration amplitude is higher on the side at all RPMs when the outer race fault is local, and the inner race fault is distributed for the same load. Irrespective of the defect type, the vibration amplitude grows as the RPM rises. Additionally, it verified that vibration amplitude invariably increases with increasing load regardless of the defect type. For unbalance in the rotor, frequency analysis reveals peak at  $1 \times \text{RPM}$  and proportional to unbalance largest in vertical direction with steady phase. Higher frequency of  $3 \times \text{RPM}$  in horizontal and vertical directions reveals to the bearing failure. As a result, the main variables in rotor-bearing systems are load and speed. The majority of the error falls within allowable limits and closely matches with the theoretical model predicted by Eq. (18) for both the vibration amplitude and the fault characteristics. Table 6 compares the performance of the rolling bearing fault detection methods. The experimental results show that the traditional method has a low fault detection rate and a detection delay, so the effect of using them for incipient

Table 5 Deterministic characteristic defective frequencies

Shaft rotation N, rpm	Rotating frequency $f_s$ , Hz	Unbalance ( $1 \times \text{RPM}$ ) Hz	Quantity of rollers Z	Compliance frequency, Hz	Defective frequency, Hz		
					$f_i$	$f_o$	$f_c$
750	15.25	12.5	29	155.6	219.7	155.2	6.62
1500	18.38	25	29	194.3	275.6	194.2	6.80
2000	22	33.33	29	231.1	329.1	231.5	8.60
3000	28	50	29	239.3	336.1	246.2	8.90



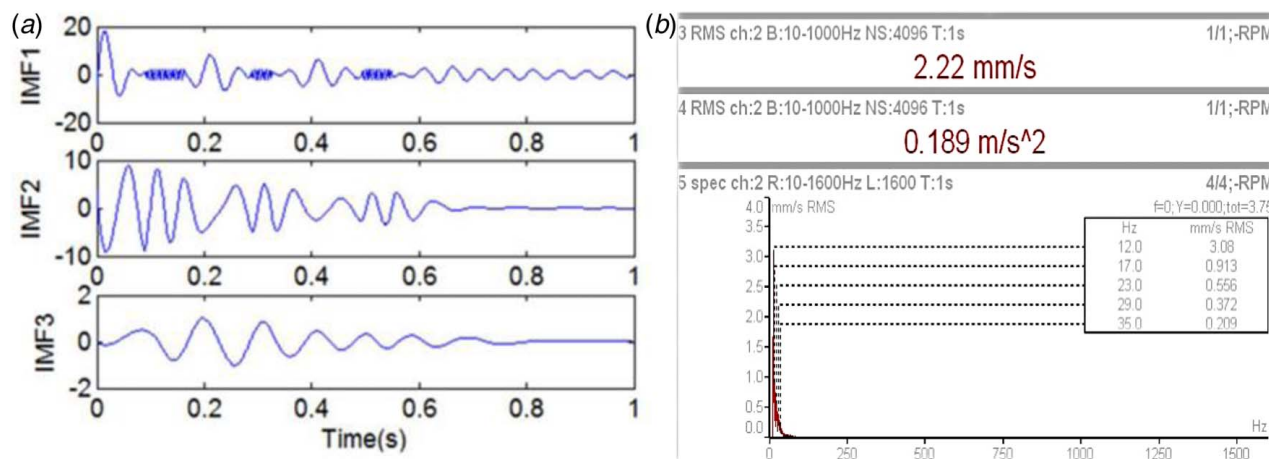


**Fig. 9 (a) IMFs of healthy bearing vibration response in time domain at 2000 rpm and (b) FFT of healthy bearing vibration response in frequency domain at 2000 rpm**

fault detection is not good. On the contrary, the HHT method has a higher fault detection rate and most of the faults can be detected and there is almost no detection delay. At the same time, the marginal Hilbert method shows better performance due to the processing of denoising.

**5.5 Validation of Model.** Fifty-four more experiments are conducted on the unbalance and varying fault sizes to confirm the validity and performance of the model with DGBB. Electric discharge machining is used to produce faults with sizes of  $5 \times 0.5 \times 0.1$  mm,  $10 \times 1.5 \times 0.3$  mm, and  $15 \times 2 \times 0.4$  mm. The proposed

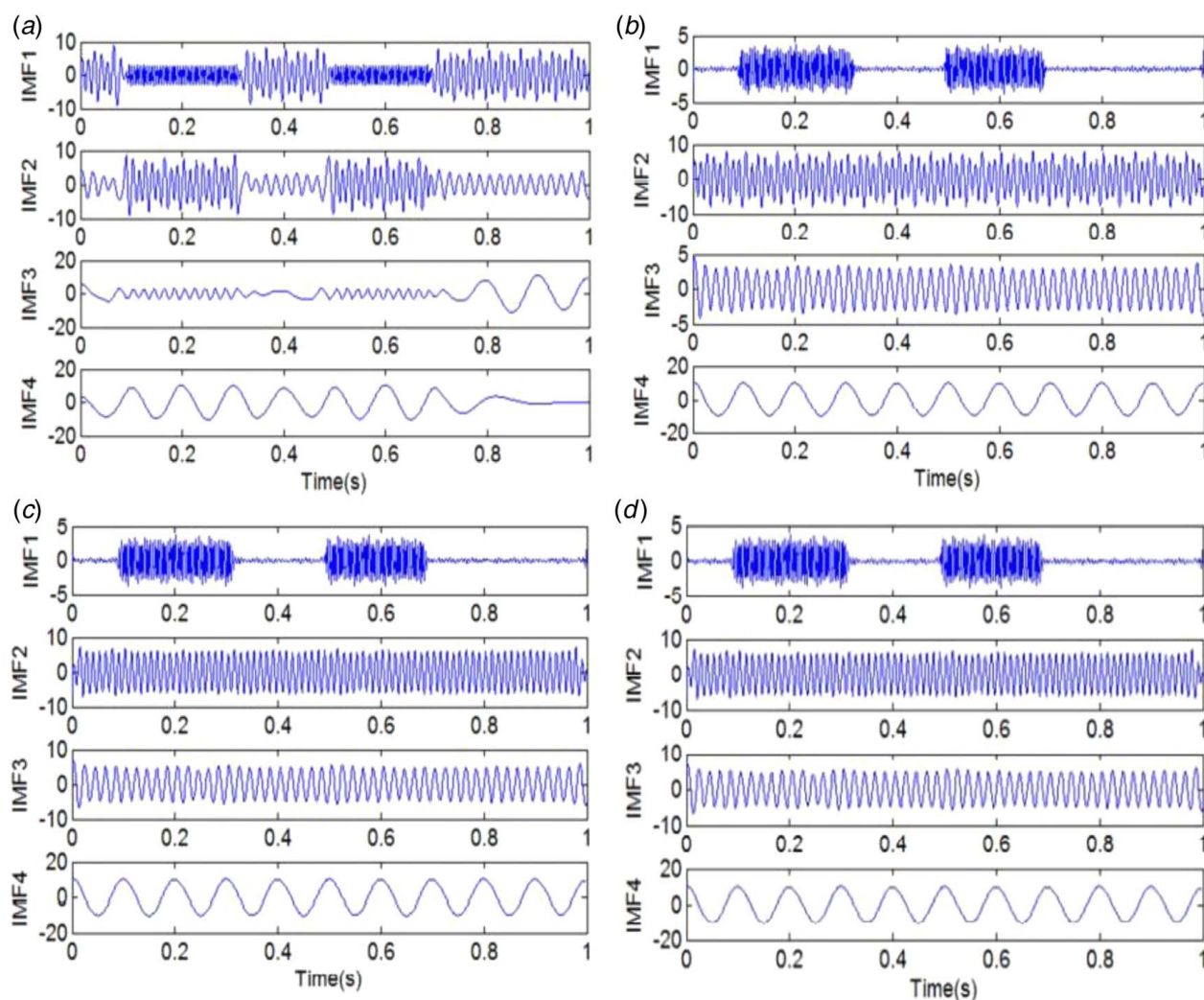


**Fig. 10 IMFs of unbalance vibration response in time domain with radial load of 500 N: (a) 750 rpm, (b) 1500 rpm, (c) 2000 rpm, and (d) 3000 rpm**

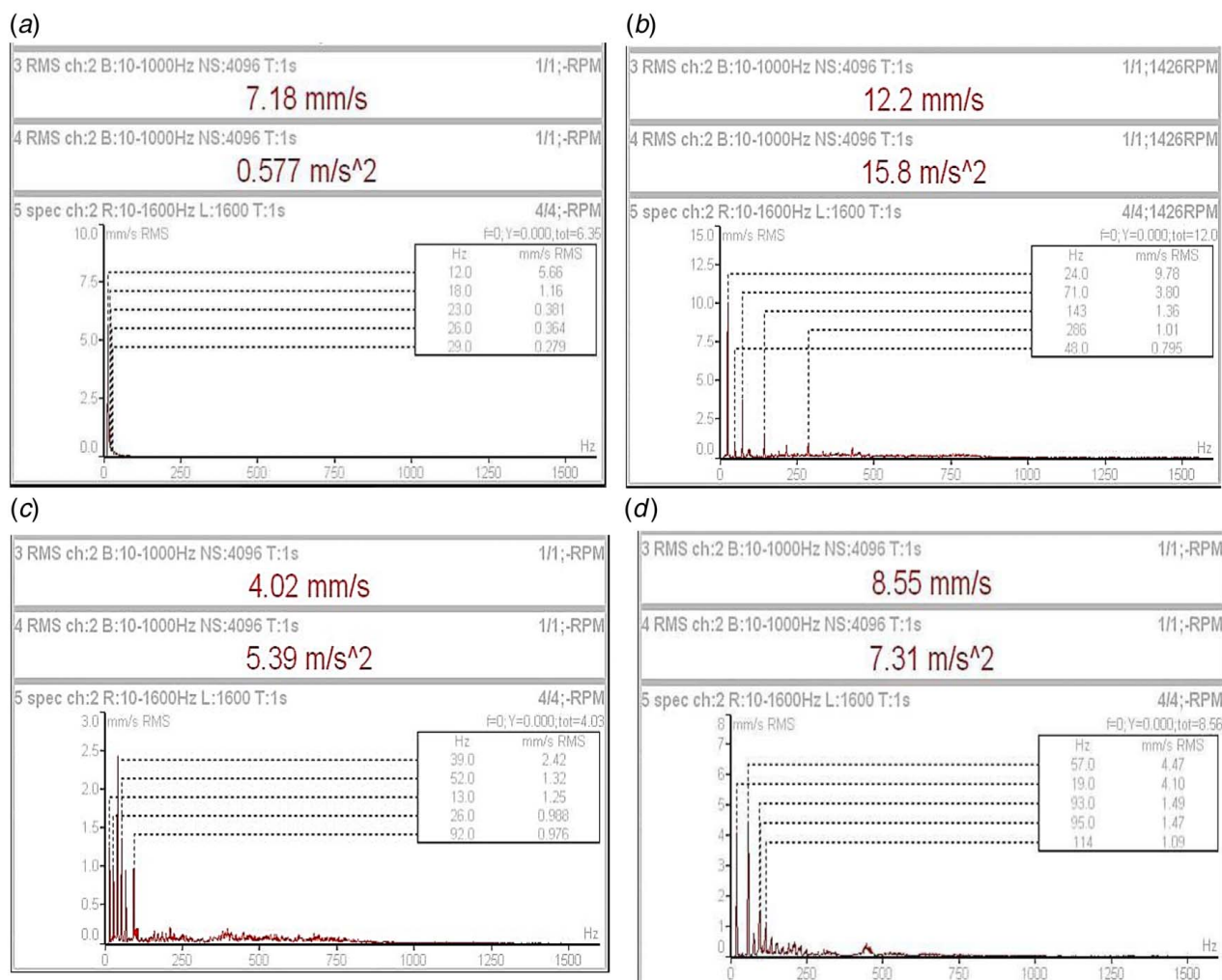


**Fig. 11** FFT unbalance vibration response in frequency domain with radial load of 500 N: (a) 750 rpm, (b) 1500 rpm, (c) 2000 rpm, and (d) 3000 rpm

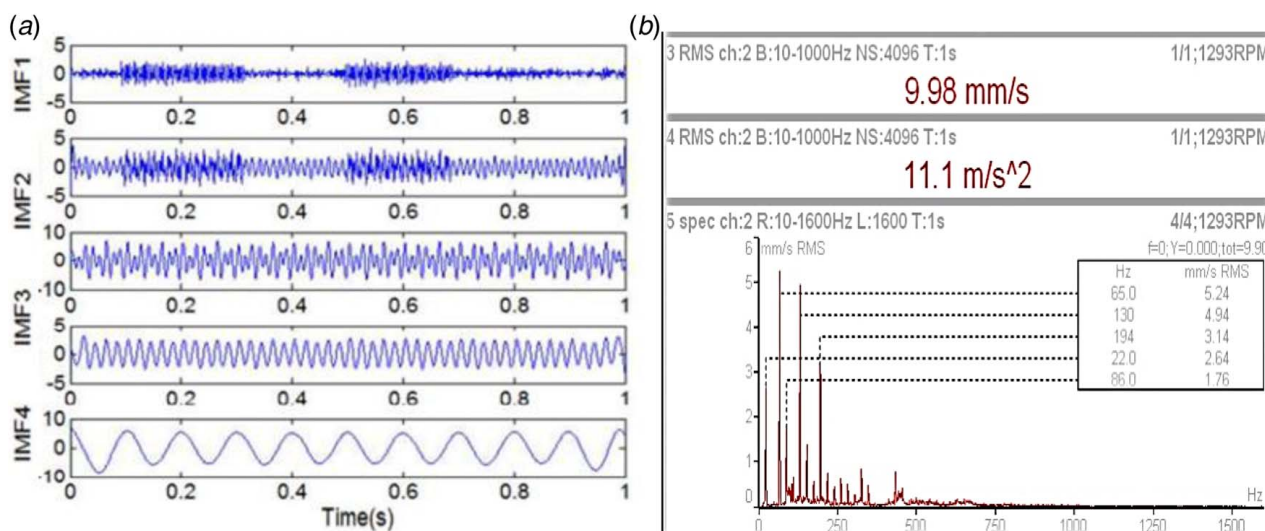


**Fig. 12** (a) IMFs of bearing outer race vibration response in time domain at 3000 rpm with radial load 500 N and (b) FFT bearing outer race vibration response in frequency domain at 3000 rpm with radial load 500 N

model, shown in Eq. (16) is utilized to compute the vibration characteristic frequencies and amplitudes. As shown in Table 7, the estimated amplitudes are analyzed with the experimentally measured

amplitudes. Table 7 compares experimental and model values for the unbalance, local outer race, outer race fault, and distributed inner race faults for various shaft rotational speeds between

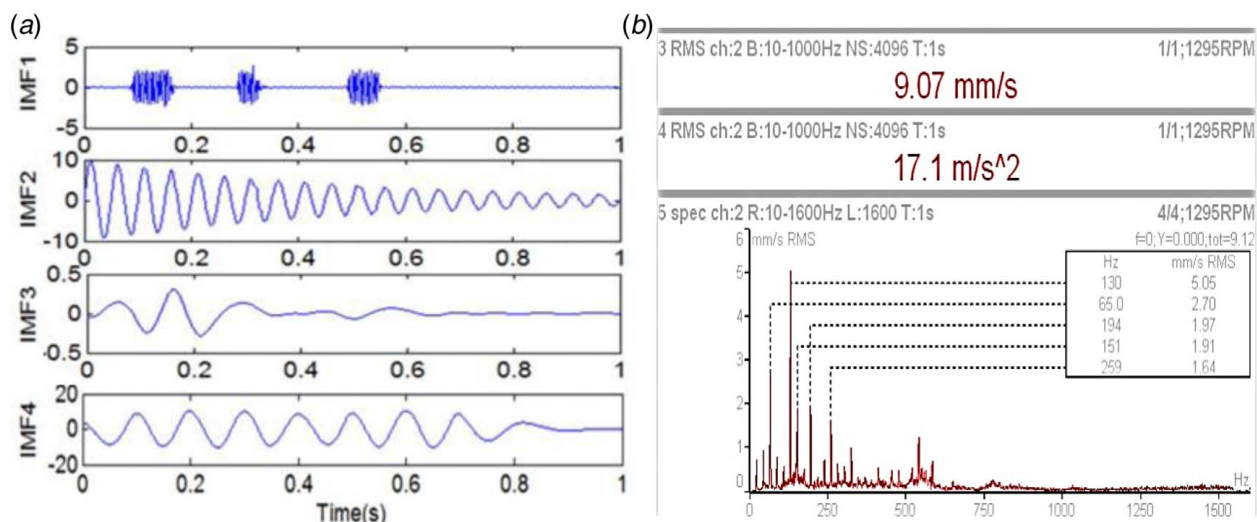


Fig. 13 (a) IMFs of bearing inner race vibration response in time domain at 3000 rpm at radial load of 500 N and (b) FFT bearing inner race vibration response in frequency domain at 3000 rpm at radial load of 500 N

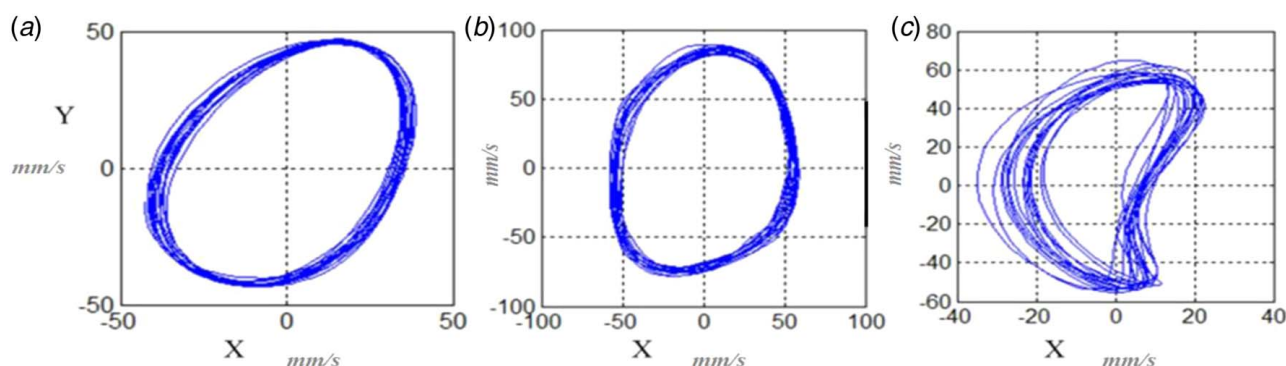


Fig. 14 Axis orbit plots of bearing under distinct operating condition: (a) normal, (b) bearing fault, and (c) unbalance

Table 6 Comparison of accuracy

Distinct technique	Features	Test reliability (%)
Morphological MH	Time domain features, ICA	88.15
WMSC-HMS	Time domain features, IMF, EMD	85.26
R-HHT	Time domain features, Pure EMD	80.98
HHT-EFD	Time and frequency domain features	79.58
HHT-Gear fault	Time and frequency domain features	67.67
HHT-Looseness	Time and frequency domain features	73.81
HHT-Unbalance	Time and frequency domain, IMF, EEMD	98.96

750 rpm and 3000 rpm, as well as the associated errors of the three cases.

A novel approach for unbalance bearing fault detection is suggested based on the findings of the experimental analysis and the results of the theoretical model. By comparing the amplitudes of two characteristic frequencies for the outer and inner races, respectively, ball pass frequency of outer race (BPFO); fundamental train frequency (FTF) and ball pass frequency of inner race (BPFI); FTF, it is possible to identify the bearing fault. Additionally, it has been found that localized faults only excite at BPFO or BPFI. There is a significant percentage of agreement between

experimental and theoretical values. With a relative error of less than 4%, the suggested model accurately predicts the behavior of unbalance bearing faults on roller bearings. Figure 15 compares the experiment and HHT with unbalance bearing fault, outer raceway, roller, and inner race. All experiments are carried out at a speed of 750–3000 rpm. The amplitude of the vibration grows together with the speed. In terms of faulty frequency, there is a strong correlation among experimental values and the HHT model. Table 8 lists the defect frequencies and amplitude determined by experiments and HHT. An excellent correlation between experimental results and the HHT model is seen.



**Table 7 Testing the validity of vibration amplitudes experiments for single disc**

Fault state	Speed (rpm)	Load	Defect frequency		Experimental trial amplitude (mm/s)	Models amplitude (mm/s)	Absolute error	Test 1		Test 2	
			H	V				Magnitude	Phase	Magnitude	Phase
Unbalance	750	100	12.1	12.6	7.18	7.35	1.23	114.31	30	114.46	29.91
	1500	200	25.2	24.3	12.2	12.8	1.36	114.36	30	114.51	29.91
	2000	300	32.8	33.3	4.02	4.23	2.12	114.40	82.5	114.55	82.69
	3000	500	50.1	50.7	8.55	8.11	2.3	114.43	82.5	114.58	82.69
Local outer race	750	100	36.1	39.3	6.69	6.23	2.45	114.45	135	114.62	135.12
	1500	200	150.2	157.9	5.12	5.81	1.23	114.48	135	114.69	135.12
	2000	300	120.6	126.7	8.45	8.12	1.58	114.49	152	114.75	152.64
	3000	500	150.2	150.3	9.98	9.51	2.10	114.50	152	114.79	152.64
Distributed Inner race	750	100	38.1	37.3	6.23	6.17	2.56	114.53	180	114.85	180.04
	1500	200	156.2	159.9	8.14	8.96	1.14	114.65	180	114.91	180.04
	2000	300	123.6	129.7	8.96	8.12	2.31	114.69	202.5	114.95	202.59
	3000	500	149.2	157.3	9.07	10.23	3.12	114.72	202.5	114.98	202.59
Roller/Ball	750	100	36.8	37.3	5.12	6.3	1.21	115	225	115.12	225.049
	1500	200	158.2	160.9	7.19	7.58	1.45	115	225	115.19	225.049
	2000	300	122.6	121.7	7.55	7.88	3.25	115	270	115.23	270.52
	3000	500	152.2	151.3	8.65	8.12	2.36	115	270	115.56	270.52

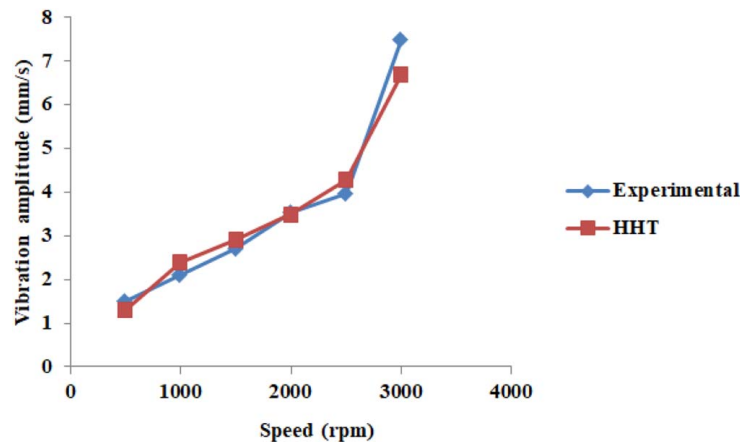


**Fig. 15 Influence of bearing fault on vibration**

**Table 8 Comparison of HHT, experimental frequencies and amplitude**

Defect position	HHT model frequency (Hz)	HHT model vibration amplitude (mm/s)	Experimental frequency (Hz)	Experimental vibration amplitude (mm/s)
Unbalance	$f_{un} = 50$	8.18	$f_{un} = 51.1$	7.18
Fault on outer race	$f_{or} = 155.4$	9.10	$f_{or} = 155.2$	9.98
Fault on inner race	$f_{ir} = 275.1$	10.01	$f_{ir} = 275.6$	9.07
Fault on roller/ball	$f_r = 36.8$	9.23	$f_r = 37.54$	10.12

## 6 Conclusion

The rolling bearing has weak incipient fault characteristics and is confused with noise, a novel method called HHT is proposed in this research work to detect the unbalance bearing fault. The fault features that are generally embedded in the intricate vibration signals can be revealed by the information contained in marginal Hilbert spectra. The fault indicator index, which is constructed by combining the M-distance index and the cosine index, can be used to improve the similarity measurements. By assessing the defect indicator indices among the marginal Hilbert spectra with the information contained, the HHT effectiveness is validated. The results of the study reveal that the similarities between the distribution

vectors of the marginal Hilbert spectrum can be classified. Integrated advanced signal processing technique of HHT with IMFs of FFT for bearing fault diagnosis. The experimental result has shown that marginal spectrum can be used as a diagnostic feature for roller bearing and used conventionally for bearing unbalance fault detection. The excellent effect of the proposed approach in fault classification is demonstrated. Additionally, the conventional technique was used to compare morphological MH, WMSC-HHT, R-HHT, HHT-EFD, HHT-Gear, and HHT-Looseness. The experimental findings show that HHT with marginal spectra has the best fault detection performance, can use more information than standard approaches, and provides accurate unbalance bearing fault detection. Through the experimental results analysis,

we can get the fault detection rate of the HHT and reaches about 97.73% and there is almost no detection delay, and thus the unbalance faults of the rotating machinery can be identified.

The HHT is a powerful tool for analyzing nonlinear and non-stationary signals. However, it also has some limitations when it comes to bearing fault detection such as sensitivity to noise, mode mixing, parameters selection, data length, and interpretability. Despite these, the HHT can be a valuable tool for bearing fault detection integrated with soft computing techniques. Future studies will test the HHT and machine learning algorithms on a wider range of mechanical items. Furthermore, the integration of more vibration and audio signals will be studied. Additionally, SVM and long short term memory (LSTM) algorithms will be used to investigate and increase the performance of the suggested technique.

## Conflict of Interest

There are no conflicts of interest.

## Data Availability Statement

No data, models, or code were generated or used for this paper.

## References

- [1] Sadeghi, F., Jalalahmadi, B., Slack, T. S., Raje, N., and Arakere, N. K., 2009, "A Review of Rolling Contact Fatigue," *ASME J. Tribol.*, **131**(4), p. 041403.
- [2] Liu, J., and Shao, Y., 2018, "Overview of Dynamic Modelling and Analysis of Rolling Element Bearings With Localized and Distributed Faults," *Nonlinear Dyn.*, **93**(1), pp. 1765–1798.
- [3] Wu, T. Y., Chung, Y. L., and Liu, C. H., 2010, "Looseness Diagnosis of Rotating Machinery Via Vibration Analysis Through Hilbert–Huang Transform Approach," *ASME J. Vib. Acoust.*, **132**(3), p. 031005.
- [4] Rai, V. K., and Mohanty, A. R., 2007, "Bearing Fault Diagnosis Using FFT of Intrinsic Mode Functions in Hilbert–Huang Transform," *Mech. Syst. Signal Process.*, **21**(6), pp. 2607–2615.
- [5] Dick, P., Carl, H., Nader, S., Alireza, M. A., and Sarabjeet, S., 2015, "Analysis of Bearing Stiffness Variations Contact Forces and Vibrations in Radially Loaded Double Row Rolling Element Bearing With Raceway Defect," *J. Mech. Syst. Signal Process.*, **50–51**(1), pp. 139–160.
- [6] Tandon, N., and Choudhury, A., 1998, "A Theoretical Model to Predict Vibration Response of Rolling Bearings to Distributed Defects Under Radial Load," *ASME J. Vib. Acoust.*, **120**(3), pp. 214–220.
- [7] Wang, Y. S., Ma, Q. H., Zhu, Q., Liu, X. T., and Zhao, L. H., 2014, "An Intelligent Approach for Engine Fault Diagnosis Based on Hilbert–Huang Transform and Support Vector Machine," *Appl. Acoust.*, **75**(1), pp. 1–9.
- [8] Huang, N. E., Shen, Z., Long, S. R., Wu, M. C., Shih, H. H., Zheng, Q., Yen, N.-C., Tung, C. C., and Liu, H. H., 1998, "The Empirical Mode Decomposition and the Hilbert Spectrum for Nonlinear and Non-Stationary Time Series Analysis," *Proc. R. Soc. London, Ser. A*, **454**(1971), pp. 903–995.
- [9] Wu, Z., and Huang, N. E., 2009, "Ensemble Empirical Mode Decomposition: A Noise-Assisted Data Analysis Method," *Adv. Adaptive Data Anal.*, **1**(1), pp. 1–41.
- [10] Ibn, S. M., and Sinha, J. K., 2016, "Rotor Unbalance Estimation With Reduced Number of Sensors," *Machines*, **4**(4), pp. 1–19.
- [11] Yu, D., Yang, Y., and Cheng, J., 2007, "Application of Time–Frequency Entropy Method Based on Hilbert–Huang Transform to Gear Fault Diagnosis," *Measurement*, **40**(9), pp. 823–830.
- [12] Song, H., Ma, W., Han, Z., and Zhu, X., 2022, "Diagnosis of Unbalanced Rolling Bearing Fault Sample Based on Adaptive Sparse Contractive Auto-Encoder and IGWO-USELM," *Measurement*, **198**(1), p. 111353.
- [13] Zhang, Y., Wang, W., Wei, D., Wang, G., Xu, J., and Liu, K., 2022, "Dynamic Stability of Unbalance-Induced Vibration in a Turbocharger Rotor-Bearing System With the Nonlinear Effect of Thermal Turbulent Lubricating Fluid Film," *J. Sound Vib.*, **528**(1), p. 116909.
- [14] Liu, H., Wang, X., and Lu, C., 2014, "Rolling Bearing Fault Diagnosis Under Variable Conditions Using Hilbert–Huang Transform and Singular Value Decomposition," *Math. Prob. Eng.*, **2014**(1), pp. 1–10.
- [15] Shinde, P. V., and Desavale, R. G., 2022, "Application of Dimension Analysis and Soft Competitive Tool to Predict Compound Faults Present in Rotor-Bearing Systems," *Measurement*, **193**(1), p. 110984.
- [16] Li, B., and Zhang, Y., 2011, "Supervised Locally Linear Embedding Projection for Machinery Fault Diagnosis," *Mech. Syst. Signal Process.*, **25**(8), pp. 3125–3134.
- [17] McFadden, P. D., and Smith, J. D., 1984, "Model for Vibration Produced by a Single Point Defect in a Rolling Element Bearing," *J. Sound Vib.*, **96**(1), pp. 69–82.
- [18] McFadden, P. D., and Smith, J. D., 1985, "Vibration Produced by Multiple Point Defects in a Rolling Element Bearing," *J. Sound Vib.*, **98**(2), pp. 263–273.
- [19] Patil, M. S., Mathew, J., Rajendrakumar, P. K., and Desai, S., 2010, "A Theoretical Model to Predict the Effect of Localized Defect on Vibrations Associated with Ball Bearing," *Int. J. Mech. Sci.*, **52**(9), pp. 1193–1201.
- [20] Igarashi, T., and Kato, J., 1985, "Studies on the Vibration and Sound of Defective Rolling Bearings. Third Report: Vibration of Ball Bearing With Multiple Defects," *Bull. JSME*, **28**(237), pp. 492–499.
- [21] Sopanen, J., and Mikkola, A., 2003, "Dynamic Model of a Deep-Groove Ball Bearings Including Localized and Distributed Defects. Part 1: Theory," *Proc. Inst. Mech. Eng., Part K*, **217**(K), pp. 201–211.
- [22] Sopanen, J., and Mikkola, A., 2003, "Dynamic Model of a Deep-Groove Ball Bearings Including Localized and Distributed Defects. Part 2: Implementation and Results," *Proc. Inst. Mech. Eng., Part K*, **217**(3), pp. 213–223.
- [23] Tandon, N., and Choudhury, A., 1997, "An Analytical Model for the Prediction of the Vibration Response of Rolling Element Bearings Due to Localized Defect," *J. Sound Vib.*, **205**(3), pp. 275–292.
- [24] Choudhury, A., and Tandon, N., 2006, "Vibration Response of Rolling Element Bearing in a Rotor Bearing System to a Local Defect Under Radial Load," *ASME J. Tribol.*, **128**(2), pp. 252–261.
- [25] Tomovic, R., Miltenovic, V., Banic, M., and Miltenovic, A., 2010, "Vibration Response of Rigid Rotor in Unloaded Rolling Element Bearing," *Int. J. Mech. Sci.*, **52**(9), pp. 1176–1185.
- [26] Desavale, R. G., Venkatachalam, R., and Chavan, S. P., 2013, "Antifriction Bearings Damage Analysis Using Experimental Data Based Models," *ASME J. Tribol.*, **135**(4), p. 041105.
- [27] Desavale, R. G., Venkatachalam, R., and Chavan, S. P., 2014, "Experimental and Numerical Studies on Spherical Roller Bearings Using Multivariable Regression Analysis," *ASME J. Vib. Acoust.*, **136**(2), p. 021022.
- [28] Desavale, R. G., Kanai, R. A., Chavan, S. P., Venkatachalam, R., and Jadhav, P. M., 2015, "Vibration Characteristics Diagnosis of Roller Bearing Using the New Empirical Model," *ASME J. Tribol.*, **138**(1), p. 011103.
- [29] Desavale, R. G., 2019, "Dynamics Characteristic and Diagnosis of a Rotor-Bearing's System Through a Dimensional Analysis Approach: An Experimental Study," *ASME J. Comput. Nonlinear Dyn.*, **14**(2), p. 014501.
- [30] Mufazzal, S., Muzzakir, S. M., and Khanam, S., 2021, "Theoretical and Experimental Analyses of Vibration Impulses and Their Influence on Accurate Diagnosis of Ball Bearing With Localized Outer Race Defect," *J. Sound Vib.*, **513**(1), p. 116407.
- [31] Patil, S. M., Desavale, R. G., Shinde, P. V., and Patil, V. R., 2020, "Comparative Study of Response of Vibrations for Circular and Square Defects on Components of Cylindrical Roller Bearing Under Different Conditions," *Lecture Notes in Mechanical Engineering Innovative Design, Analysis and Development Practices in Aerospace and Automotive Engineering*, N. Gascoin and E. Balasubramanian, eds., Springer, New York, pp. 189–198.
- [32] Kanai, R. A., Desavale, R. G., and Chavan, S. P., 2016, "Experimental-Based Fault Diagnosis of Rolling Bearings Using Artificial Neural Network," *ASME J. Tribol.*, **138**(3), p. 031103.
- [33] Patel, V. N., Tandon, N., and Pandey, R. K., 2010, "A Dynamic Model for Vibration Studies of Deep Groove Ball Bearings Considering Single and Multiple Defects in Races," *ASME J. Tribol.*, **132**(4), p. 041101.
- [34] Jing, L., 2020, "A Dynamic Modelling Method of a Rotor-Roller Bearing-Housing System With a Localized Fault Including the Additional Excitation Zone," *J. Sound Vib.*, **469**(1), p. 115144.
- [35] Linkai, N., Hongrui, C., Huipeng, H., Bing, W., Yuan, L., and Xiaoyan, X., 2020, "Experimental Observations and Dynamic Modeling of Vibration Characteristics of a Cylindrical Roller Bearing With Roller Defects," *J. Mech. Syst. Signal Process.*, **138**(1), pp. 1–19.
- [36] Rafsanjani, A., Abbasion, S., Farshidianfar, A., and Moeenfar, H., 2009, "Nonlinear Dynamic Modeling of Surface Defects in Rolling Element Bearing Systems," *J. Sound Vib.*, **319**(3–5), pp. 1150–1174.
- [37] Rui, Y., Lei, H., Yulin, J., Yushu, C., and Zhiyong, Z., 2018, "The Varying Compliance Resonance in a Ball Bearing Rotor System Affected by Different Ball Numbers and Rotor Eccentricities," *ASME J. Tribol.*, **140**(5), p. 051101.
- [38] Jadhav, P. M., Kumbhar, S. G., Desavale, R. G., and Patil, S. B., 2020, "Distributed Fault Diagnosis of Rotor-Bearing System Using Dimensional Analysis and Experimental Methods," *Measurement*, **166**(1), p. 108239.
- [39] Kumbhar, S. G., Sudhagar, E. P., and Desavale, R. G., 2020, "Theoretical and Experimental Studies to Predict Vibration Responses of Defects in Spherical Roller Bearings Using Dimension Theory," *Measurement*, **161**(1), p. 107846.
- [40] Kumbhar, S. G., and Sudhagar, E. P., 2020, "Fault Diagnostics of Roller Bearings Using Dimension Theory," *ASME J. Non. Eval. Diag. Prog. Eng. Syst.*, **4**(1), p. 011001.
- [41] Salunkhe, V. G., Desavale, R. G., and Jagadeesha, T., 2021, "Experimental Frequency-Domain Vibration Based Fault Diagnosis of Roller Element Bearings Using Support Vector Machine," *ASCE-ASME J. Risk Uncertainty Eng. Syst., Part B: Mech. Eng.*, **7**(2), p. 021001.
- [42] Shinde, P. V., Desavale, R. G., Jadhav, P. M., and Sawant, S. H., 2023, "A Multi Fault Classification in a Rotor-Bearing System Using Machine Learning Approach," *J. Braz. Soc. Mech. Sci. Eng.*, **45**(2), p. 121.
- [43] Vishwendra, M. A., Salunkhe, P. S., Patil, S. V., Shinde, S. A., Shinde, P. V., Desavale, R. G., Jadhav, P. M., and Dharwadkar, N. V., 2022, "A Novel Method to Classify Rolling Element Bearing Faults Using K-Nearest Neighbor Machine Learning Algorithm," *ASCE-ASME J. Risk Uncertainty Eng. Syst., Part B: Mech. Eng.*, **8**(3), p. 031202.
- [44] Mohanty, A. R., 2018, *Machinery Condition Monitoring: Principles and Practices*, CRC Press, Boca Raton, FL.
- [45] Hertz, H., 1881, "On the Contact of Elastic Solids," *J. Reine. Angew. Math.*, **92**(1), pp. 156–171.